Conformational Response of N-Terminally Truncated Cytochrome P450 3A4 to Ligand Binding in Solution

Shih-Wei Chuo,[†] Shu-Hao Liou,[†,⊥] Lee-Ping Wang,[†] R. David Britt,[†] Thomas L. Poulos,[‡,§,∥] Irina F. Sevrioukova,[‡] and David B. Goodin*,[†]

[†]Department of Chemistry, University of California, Davis, One Shields Avenue, Davis, California 95616, United States

[‡]Department of Molecular Biology and Biochemistry, University of California, Irvine, California 92697-3900, United States

[§]Department of Chemistry, University of California, Irvine, California 92697-3900, United States

[∥]Department of Pharmaceutical Sciences, University of California, Irvine, California 92697-3900, United States

[⊥]Department of Anatomy and Structural Biology, Albert Einstein College of Medicine, Bronx, New York 10461, United States

S *Supporting Information*

ABSTRACT: Human cytochrome P450 3A4 (CYP3A4) is a membrane-associated monooxygenase that is responsible for metabolizing >50% of the pharmaceuticals in the current market, so studying its chemical mechanism and structural changes upon ligand binding will help provide deeper insights into drug metabolism and further drug development. The best-characterized cytochrome P450 is a bacterial form, P450cam, which undergoes significant conformational changes upon binding substrate and its redox partner, putidaredoxin. In contrast, most crystal structures of CYP3A4 with or without ligands have shown few changes, although allosteric effects and multiple-substrate binding in solution are well-documented. In this study, we use double electron−electron resonance (DEER) to measure distances between spatially separated spin-labels on CYP3A4 and molecular dynamics to interpret the DEER data. These methods were applied to a soluble N-terminally truncated CYP3A4 form, and the results show that there are few changes in the average structure upon binding ketoconazole, ritonavir, or midazolam. However, binding of midazolam, but not ketoconazole or ritonavir, resulted in a significant change in the motion and/or disorder in the F/G helix region near the substrate binding pocket. These results suggest that soluble CYP3A4 behaves in a unique way in response to inhibitor and substrate binding.
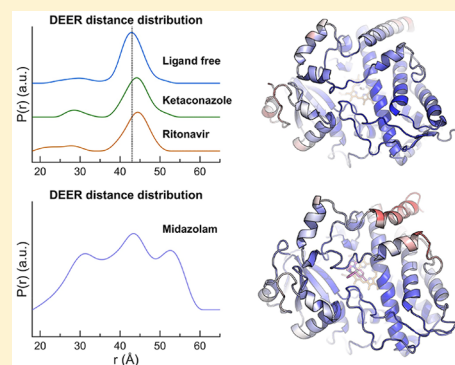
Members of the cytochrome P450 (CYP) superfamily are heme-containing monooxygenases that insert a single oxygen atom into a wide variety of organic molecules. Cytochrome P450 3A4 (CYP3A4) is a membrane protein expressed in human liver and intestine. Human CYP3A4 contributes to the metabolism of >50% of all drugs in clinical use and thus is of considerable clinical significance.[1] Because many drugs are hydrophobic, the insertion of an oxygen improves water solubility for easier excretion. In general, endogenous substrates and xenobiotics are termed type I or type II ligands on the basis of the triggered ultraviolet−visible (UV−vis) spectral changes in the heme Soret absorption.[2] Type I ligands displace water as the sixth ligand coordinated to the heme iron, which shifts the ferric (Fe^{3+}) iron from low-spin to high-spin, resulting in a blue shift in the Soret band. This ligand-induced change often increases the oxidation−reduction potential,[3,4] thereby promoting electron transfer from its reductase to initiate the P450 catalytic cycle. On the other hand, type II ligands induce a red shift in the Soret band by direct coordination to the heme iron and thus are often inhibitors of P450 activity.

Although some P450 isoforms, such as CYP2B4, have been observed in different conformational states in response to ligand binding,[5−7] not all mammalian CYP enzymes have shown such changes.[8−12] Studies of membrane-bound CYP enzymes are challenging because the proteins tend to aggregate in an aqueous environment. Thus, forms containing truncations of the N-terminal transmembrane segment as well as detergents and liposomes have been utilized to obtain homogeneous preparations. Since 2004, a number of ligand-bound and ligand-free crystal structures of Δ3−22 CYP3A4 have been determined.[13−16] These structures showed that CYP3A4 shares a global fold with other P450s but has a longer F−G peptide, consisting of short F, F′, G′, and G helices and connecting loops that comprise the roof of the active site. As the currently available crystal structures make evident, the CYP3A4 active site is large enough to accommodate structurally diverse ligands, most of which trigger only a small conformational change.[13−16] Among the wide variety of

substrates oxidized by CYP3A4, midazolam (MDZ) is particularly important because it is selectively metabolized by CYP3A4 and is used as an *in vivo* marker substrate for clinical studies.[17] The crystal structure of the MDZ−CYP3A4 complex is the only example of a substrate-induced reshaping of the CYP3A4 active site.[18] Upon formation of the MDZ−CYP3A4 complex, most of the structure including the A helix remains the same, while the N-terminus of helix G is partially unwound. Structural studies have also been conducted on human CYP3A4 complexed with type II ligands, including ketoconazole (KET) and ritonavir (RIT),[19,20] whose direct coordination to the heme iron leads to a decrease in redox potential and inhibition of catalysis. In these cases, only minor conformational changes in the F, F′, G, and G′ helices were observed in both structures compared to ligand-free CYP3A4 [Protein Data Bank (PDB) entry 5vcd structure].

There is some evidence that the membrane or detergent environment surrounding the protein may affect its conformational response to ligand binding. In a recent study, an anion binding site was observed at the N-terminus of Δ3−22 CYP3A4, which is suitable for interaction with the head groups of negatively charged phospholipids and showed an enhanced substrate-induced low-spin to high-spin transition in the presence of anions.[21] In addition, the Δ3−12 N-terminally truncated CYP3A4 was observed to undergo an enhanced low-spin to high-spin conversion upon ligand binding in lipid nanodiscs, a model membrane system that can mimic a nativelike membrane bilayer.[22,23] The larger spin shift could indicate a more extensive conformational change taking place in a membrane environment and/or simply be due to the higher temperature, 37 °C, used for these studies.

It thus is of fundamental importance to determine ligand-induced structural changes in CYP3A4 in solution and how they depend on the protein environment. In this study, double electron−electron resonance (DEER) was coupled with site-directed spin labeling (SDSL) to monitor the distance between a pair of spin-labels designed to report on conformational changes in the G and G′ helices in response to ligand binding. In addition, molecular dynamics (MD) was applied to interpret DEER distance measurements and spin-label rotamers, and DEER distances were used with restrained MD to assess the relative contribution of main-chain and side-chain rotamer populations that give rise to the observed DEER measurements.

■ EXPERIMENTAL PROCEDURES

Protein Expression and Purification. Cysteine-depleted Δ3−22 CYP3A4 was used as a template to produce the M59C/R243C and M59C/E63C-I232C/V235C mutants, which were expressed and purified as described previously.[24]

Spin Labeling and EPR Sample Preparation. (1-Oxyl-2,2,5,5-tetramethylpyrroline-3-methyl) methanethiosulfonate (MTSL) and 3,4-bis(methanethiosulfonylmethyl)-2,2,5,5-tetramethyl-2,5-dihydro-1*H*-pyrrol-1-yloxy spin-label (BSL) were purchased from Toronto Research Chemicals. Before labeling, the protein sample was loaded onto a PD-10 column for removal of dithiothreitol. A 10-fold molar excess of spin-label was added to the cysteine-mutated CYP3A4. The sample was incubated at room temperature for 1 h, followed by six concentration/dilution cycles using an ultrafiltration membrane with 150 mM KCl, 100 mM potassium phosphate, and 20% glycerol (pH 7.1, pD 7.5) to remove excess spin-label. After spin-label attachment, samples were incubated with the desired ligand at room temperature for 1 h, and 0.7% CHAPS was introduced to prevent aggregation.

EPR and DEER Spectroscopy. X-Band CW-EPR measurements were performed on a Bruker Elexsys E500 spectrometer with a superhigh Q resonator (ER4122SHQE). The low-spin and high-spin EPR spectra were obtained with a modulation frequency of 100 kHz at 50 K and 0.2 mW and at 15 K and 2 mW, respectively. For all CW-EPR measurements, standard 4 mm quartz tubes from Wilmad were used. DEER spectra were recorded at Q-band (34 GHz) on a Bruker E580 spectrometer with a Bruker EN5107D2 Q-band EPR/ENDOR probe-head using the four-pulse sequence $\pi/2(\nu_{probe}) \rightarrow \tau_1 \rightarrow \pi(\nu_{probe}) \rightarrow (\tau_1 + T) \rightarrow \pi(\nu_{pump}) \rightarrow (\tau_2 - T) \rightarrow \pi(\nu_{probe}) \rightarrow \tau_2 \rightarrow$ echo, where T was advanced in 20 ns steps. The $\pi/2$ and π pulse lengths at the probe frequency were 16 and 32 ns, respectively, and the π pulse length at the pump frequency was usually 16 or 20 ns, determined by a separate nutation experiment. The difference between the probe and pump spin frequency was 80 MHz, and the temperature was set to 20 K to optimize the spin-label relaxation time. After the DEER data had been recorded, all traces were analyzed by the DeerAnalysis2016 software package.[25] After background subtraction, Tikhonov regularization using L curves was used to construct distance distributions. A validation tool in DeerAnalysis2016 was used to evaluate the sensitivity of distance peaks on the analysis parameters (see the Supporting Information).

Spin-Label Partial Charges. To calculate partial atomic charges on MTSL and BSL containing covalent cysteine links, spin-label-attached cysteines were capped with acetyl (ACE) and *N*-methylamine (NME) residues on their N-terminal and C-terminal ends, respectively. Geometry optimization was performed using the Gaussian09 series of programs[26] at the *ab initio* Hartree−Fock level with the standard 6-31G* basis set, and the antechamber package[27] was used for restrained electrostatic potential (RESP) charge fitting.[28]

Molecular Dynamics (MD). Two initial structures of substrate-free and MDZ-bound CYP3A4 were obtained from the Protein Data Bank (entries 1tqn and 5te8, respectively).[15,18] All six non-heme-ligating cysteines were mutated to generate the cysteine-depleted CYP3A4, and M59C/R243C and M59C/E63C-I232C/V235C were added for MTSL and BSL labeling. The force field for ferric high-spin and low-spin heme was calculated using the MCPB.py model in AMBER16.[29] The general Amber force field (GAFF)[30] was applied for MDZ, and its partial atomic charges were calculated by the same method that was used for spin-labels. All crystallographic waters were retained in each structure, and the Amber ff14SB force field[31] was used on the protein in all MD simulations. Each structure was solvated within a periodic truncated octahedral box with TIP3P type waters using a 10 Å cushion, and chloride ions were added to maintain the neutral charge. The simulations start with energy minimization by the steepest descent algorithm for 10000 steps with 100 kcal mol^{-1} Å^{-2} harmonic restraints on the protein followed by another energy minimization with restraints on heavy atoms, and the system was heated smoothly from 0 to 300 K. Before the final 100 ns production run, a 7 ns equilibrium was carried out with gradual release of restraints on the protein backbone. The MD trajectory that resulted in the most representative conformation was analyzed using the hierarchical clustering algorithm from the AMBERTOOLS package.[32] All MD simulations were carried out using the GPU compatible Amber16 software package.[33]
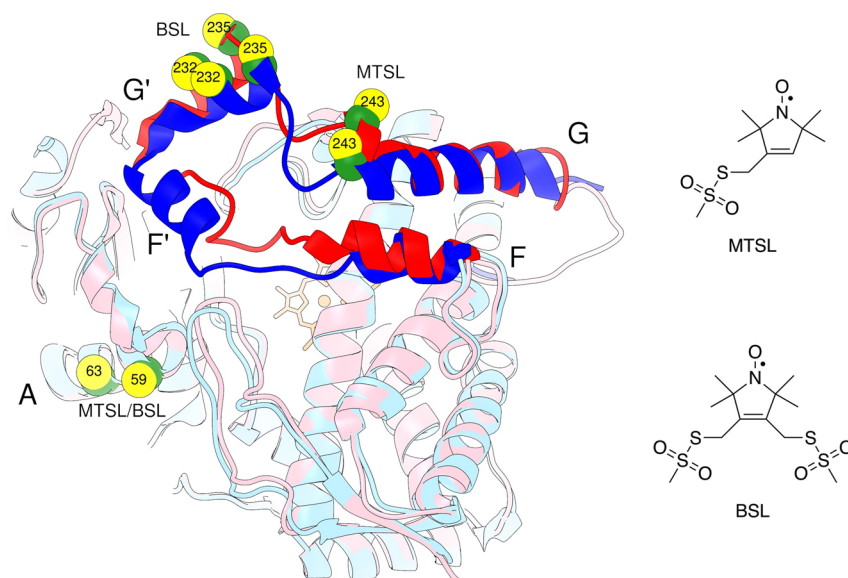
Figure 1. Positions of labeling sites for MTSL and BSL in Δ3−22 CYP3A4 to probe G and G′ helix movements. Shown are the crystal structures of ligand-free (PDB entry 5vcd, light blue) and MDZ-bound (PDB entry 5te8, pink) forms. The C_β atoms of M59C/R243C and M59C/E63C-I232C/V235C are shown as yellow spheres, and the heme is shown as orange sticks. F, F′, G′, and G helices in the ligand-free and MDZ-bound forms are colored blue and red, respectively. Chemical structures of nitroxide spin-labels (MTSL and BSL) used in this study are shown on the right.
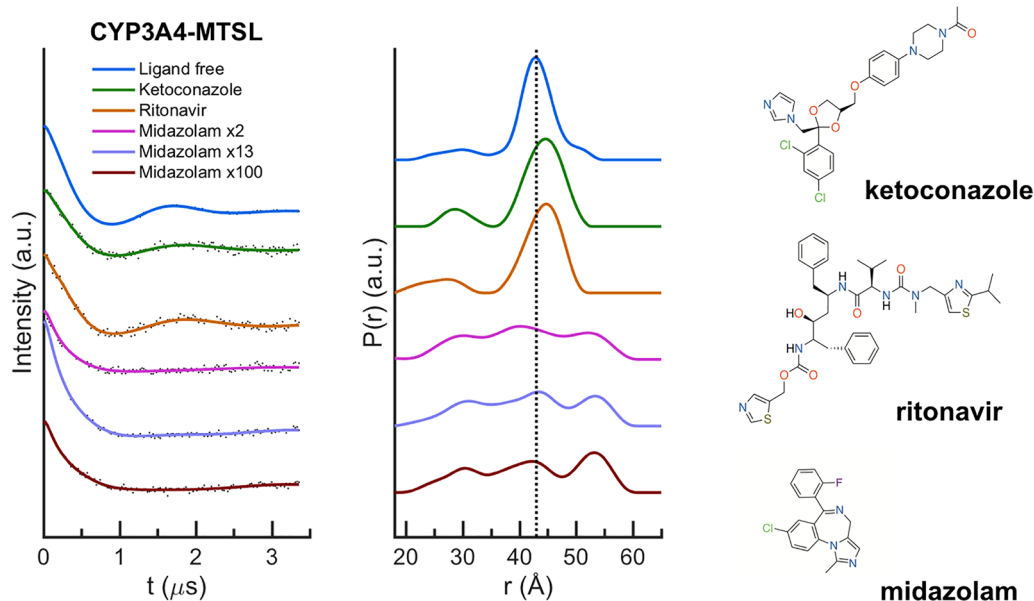

Figure 2. Time-domain DEER data and distance distribution of CYP3A4 with MTSL for different ligand-bound states. Raw DEER echo amplitudes after background subtraction are shown as points, and the solid traces are the fitted curves. The dotted line indicates a DEER distance of 43 Å for the ligand-free state. Chemical structures of the ligands are shown on the right.

■ RESULTS

A Spin-Label Probe for Movements of the G and G′ Helices. On the basis of previous structural studies,[13,15,16,18,19,24] sites were designed on Δ3−22 CYP3A4 for the placement of pairs of MTSL and BSL spin-labels. For MTSL labeling, residue M59 was chosen as an immobile reference site on the A helix, and R243 on the G helix was selected to probe movements of the G and G′ helices. As shown in Figure 1, to incorporate MTSL spin-labels, the M59C and R243C mutations were introduced into cysteine-depleted CYP3A4, while the construct M59C/E63C-I232C/V235C was used to introduce bifunctional spin-labels (BSLs). Protein

samples were purified and labeled for initial characterization, and the results indicated the presence of aggregated states, necessitating the use of detergents. CHAPS is a zwitterionic detergent that has been widely used for solubilization of membrane proteins. The combined features of a bile acid salt and an alkyl sulfobetaine make it effective in breaking protein−protein interactions without denaturation. Figure S1 shows gel filtration data indicating that the Δ3−22 N-terminal deletion mutant of CYP3A4 forms aggregates in the absence of a detergent but becomes a monodisperse monomer at concentrations of CHAPS (0.7%) that are at or above the critical micelle concentration. Heterogeneity due to CYP3A4

Table 1. Comparison of Distances (in angstroms) in Different Ligand-Bound Forms of CYP3A4[a]

	crystal 59Cα−243Cα	DEER (MTSL)	MD (MTSL)	DEER (BSL)	MD (BSL)
ligand-free	33.3 (5vcd)	43	43	46.9	47.4
midazolam	36.7/37.4/36.9 (5te8)	31/43/52	29.6/41.5		
ketoconazole	33.2/33.8/33.0 (2v0m)	44		47.6	
ritonavir	32.8/32.9 (3nxu)	44		47.3	

[a]Crystal distances were measured between the Cα atoms at the labeling site, and the DEER and MD distances were measured between the nitroxide spin-labels; therefore, the length and orientation of the spin-label side chain need to be taken into account between crystal and DEER distances.

aggregation and dimerization could certainly complicate the DEER analysis, so all DEER samples for this study were prepared in the presence of 0.7% CHAPS.

Effect of CHAPS on CYP3A4 Ligand Binding. UV−vis spectral measurements (Figure S2) indicate that in the ligand-free state, the presence of 0.7% CHAPS caused a small perturbation in the heme Soret band suggesting a partial low-spin to high-spin conversion. Figure S2 also shows that addition of the inhibitors KET and RIT results in reversion to low-spin spectra even in the presence of CHAPS as expected for these type II ligands. Titration of MTSL-labeled Δ3−22 CYP3A4 containing 0.7% CHAPS with the type I substrate MDZ converts the enzyme to a high-spin state with an apparent K_d value of 18.4 μM (Figure S3). This is 3.8-fold higher than previously reported in the absence of CHAPS[18] but otherwise demonstrates that MDZ binds to the MTSL-labeled enzyme to give the expected high-spin complex.

These results are supported by the CW-EPR spectra (Figures S4 and S5). As shown in Figure S4, the ligand-free form gives a low-spin signal with a g_z of 2.41 that becomes somewhat broadened and possibly split in the presence of 0.7% CHAPS. In agreement with the UV−vis data, the ligand-free state shows a small amount of high-spin EPR signal at approximately g = 8.22 in the presence of CHAPS (Figure S5). Addition of KET or RIT causes the appearance of unique low-spin signals with g_z values of 2.48 and 2.47, respectively (Figure S4), showing that these inhibitors make specific interactions with the heme as expected for type II ligands.[34,35] However, addition of a 2- or 13-fold molar excess of MDZ results in the nearly complete disappearance of the low-spin signal (Figure S4) and the appearance of a high-spin EPR signal at g = 8.22 (Figure S5). Only a small amount of a low-spin signal at g_z = 2.4 for 2× MDZ or g_z = 2.48 for 13× MDZ remains. The 2× MDZ and 13× MDZ EPR samples were prepared with 100 μM CYP3A4. Thus, the concentration of free MDZ for both samples is far higher than K_d, and we can thus conclude that MDZ binding is virtually complete. Finally, we examined the effect of a much larger excess of MDZ. Figures S6 and S7 show low-spin and high-spin EPR spectra, respectively, for 50 μM CYP3A4 and a 100-fold molar excess of MDZ. A low-spin signal is seen at g_z = 2.47 in addition to the high-spin signal. This suggests that a large excess of MDZ may partially convert the high-spin complex to a low-spin form that is distinct from the ligand-free state, which could be due to binding of multiple MDZ molecules to the active site.

Ligand-Dependent Structural Changes in CYP3A4. Figure 2 shows the effect of KET, RIT, and MDZ binding on the distance between spin-labels measured by DEER in CYP3A4 labeled with MTSL. The ligand-free sample results in a well-defined modulation with a single dominant distance at 43 Å. Both KET- and RIT-bound states have the most probable distance of 44 Å, which is approximately 1 Å longer

than in the ligand-free state and consistent with X-ray crystallography that showed only minor changes (Table 1). Interestingly, we also introduced BSLs into this site using the C59/C63-C232/C235 mutant and also observed a 1 Å shift after KET and RIT binding (Figure 3). Therefore, this
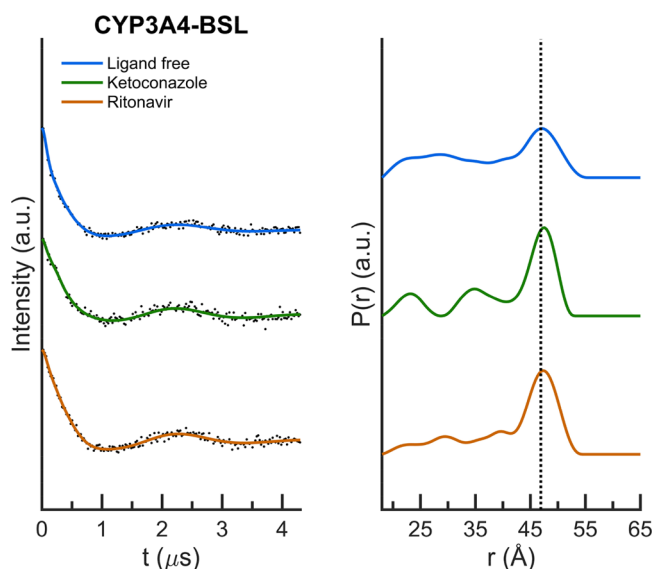

Figure 3. Time-domain DEER data and distance distribution of CYP3A4 with BSL for different ligand-bound states. Raw DEER echo amplitudes after background subtraction are shown as points, and the solid traces are the fitted curves. The dotted line indicates a DEER distance of 47.4 Å for the ligand-free state.

approximately 1 Å longer distance for the inhibitor-bound states is confirmed by two distinct labeling strategies. In contrast, for the smaller substrate MDZ, multiple peaks at 31, 43, and 52 Å are observed in the DEER distance distributions as shown in Figure 2. The fact that no single distance dominates in the MDZ-bound forms is a consequence of the overall loss of modulation amplitude in the time-domain DEER data. This in turn suggests that the position of the three weaker peaks observed in the MDZ complexes may not be accurately determined. Furthermore, analysis of the distance distribution profiles as a function of analysis parameters (Figure S8) shows that the peak at 52 Å is heavily dependent on analysis parameters and thus may not be reliable. These results strongly suggest that the MDZ-bound state is more heterogeneous than the KET or RIT complexes, with a number of distances contributing and no single one dominating. While the crystal structure of MDZ-bound CYP3A4 shows a 3.4−4.1 Å longer distance between the Cα atoms of M59 and R243 compared to that of the ligand-free state (Table 1), our DEER analysis suggests that MDZ binding induces a significant increase in the level of disorder in the G helix region. Because
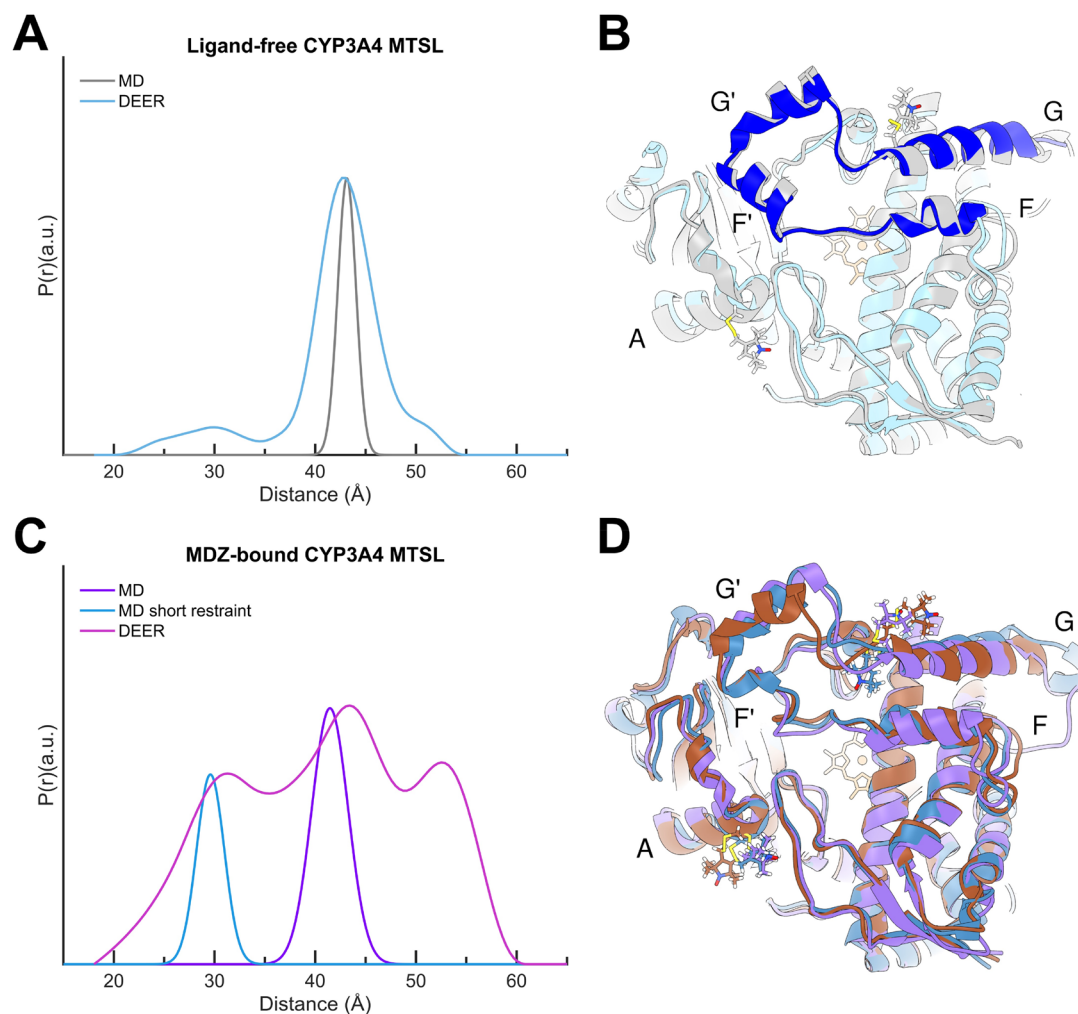
Figure 4. (A and C) Comparison of MD and DEER distance distributions for ligand-free and MDZ-bound states, respectively. (B and D) MD structures from cluster analysis of MD trajectories for ligand-free and MDZ-bound states, respectively. The ligand-free crystal structure (5vcd) is colored blue, and its MD structure is colored gray. Three MDZ-bound MD structures are colored brown, purple, and blue, corresponding to longer, intermediate, and shorter DEER distance distributions, respectively.

this heterogeneity might be caused by multiple MDZ molecules binding, we compared samples containing 13- and 100-fold excesses of MDZ.[18] None of the MDZ samples showed clear evidence of DEER modulation (Figure 2).

Molecular Dynamics Simulation. To help interpret the DEER distances seen in Figure 2, we used MD calculations to provide predictions of the effects of ligands on the spin-label distance. MD distance distributions between nitroxide nitrogens on MTSL were calculated from 100 ns MD simulations for ligand-free and MDZ-bound CYP3A4. The MSTL distances of ligand-free CYP3A4 distances predicted by MD and DEER match very well (Figure 4A and Table 1). Although the distance distribution width seen by DEER is larger than that suggested by MD, the peak values differ by <0.12 Å, and the structure shown in the most representative cluster has a conformation essentially identical to the crystal structure (Figure 4B). This gives us a high degree of confidence that the ligand-free state in solution is accurately represented in the crystal structure.

MD calculations were also used in an attempt to gain insight into the multiple peaks observed for the MDZ complex. In the MDZ-bound state, the DEER data suggest multiple distances, including peaks at 31, 43, and 52 Å, although the longer one

may be unreliable as indicated above. Initial MD simulations for the MDZ-bound form gave a distance of 41.5 Å (Table 1), which agrees fairly well with the intermediate distance. To account for the shorter and longer distances of ~31 and ~52 Å, respectively, distance-restrained MD calculations on the MDZ-bound state were performed. In each case, the starting state was the MDZ-bound structure (5te8). After minimization and annealing steps, equilibrium and production runs were performed with the spin-labels restrained to their DEER observed distances, followed by a gradual restraint release and 100 ns of unrestrained MD. For the shorter distance, a state with a distance of 29.6 Å remained stable after the restraints had been removed, and this corresponds to a protein structure in which the end of the G helix is very similar to that in the ligand-free conformation but with an alternate spin-label rotamer (Figure 4C,D). On the other hand, for the longer distance, the restrained MD structure initially agreed with the DEER result, but this was not stable and reverted to the 43 Å distance over ~15 ns of unrestrained MD (Figure S9). Most of this change is attributed to a movement of the "reference" MTSL (residue 59) rotamer position (Figure 4D), so our MD runs suggest that pushing the spin-labels apart to the 52 Å distance results in an unstable rotamer of the reference spin-

label at residue 59 that relaxes upon release of the restraint. Thus, MD does not account for the 52 Å distance seen in our DEER result. This is consistent with our suggestion above that the longer DEER distance peak observed for the MDZ complexes may be artifactual. Interestingly, in our MD runs for the MTSL-labeled MDZ–CYP3A4 complex, the N-terminus of the G helix is straight (Figure 4D) instead of slightly bent as seen in the crystal structure (Figure 1). In addition, the MDZ-bound CYP3A4 distance distribution width suggested by MD is wider than that in the MD simulation of the ligand-free state, with the full widths at half-maximum being 4.27 and 2.04 Å, respectively. These latter two observations support the idea that the MDZ-bound state is more mobile or exists in multiple states relative to the ligand-free form.

For BSLs attached to C59/C63-C232/C235, our average MD distance for ligand-free CYP3A4 is within 0.68 Å of the dominant DEER distance, and the conformation of the most representative structure is essentially identical to the crystal structure (Figure S10A, 10B). Figure S10C shows that the cluster of states sampled by MD suggests that the mobility of the label on the G′ helix is significantly larger than on the reference site. Still, the MD simulations suggest a narrower distribution of states than seen by DEER. Overall, there is very good agreement with the absolute distance, which gives us confidence that the DEER-reported conformation of the substrate-free form is the same as that in the crystal.

DISCUSSION

The large binding pocket is an important structural feature of CYP3A4, allowing it to accommodate a vast range of substrates. However, the role of conformational flexibility in substrate recognition and its extent are not completely understood. It is possible that intermolecular contacts in the crystal lattice may select one conformation from an ensemble of sampled states, e.g., through the outer surface of the hydrophobic F′ and G′ helices.[36,37] Therefore, it is important to investigate how CYP3A4 behaves upon ligand binding in solution. To compare the effect of type I or type II ligand binding on the conformational dynamics of CYP3A4, we performed DEER for the N-terminally truncated CYP3A4 bound to KET, RIT, and MDZ. For the bulky type II ligands, one prominent distance peak is observed at 44 Å with a relatively narrow distance distribution. The 1 Å distance increase compared to ligand-free CYP3A4 is consistent with the previous crystal structures that show only modest changes near the G helix. KET and RIT exhibit significant configurational entropy because of multiple rotatable bonds but, nonetheless, bind to CYP3A4 with high affinity. In the co-crystal structures with CYP3A4, both ligands form van der Waals contacts and hydrophobic interactions with the hydrophobic pocket and directly ligate to the heme iron. This helps to stabilize the inhibitory complex and explains why CYP3A4 bound to type II ligands has a relatively rigid structure compared to that of the complex with the smaller type I ligand, MDZ. In addition, the DEER distance profiles in ligand-free samples have a narrower distance distribution, with a shift in the most probable distance instead of multiple and wider distance distributions as seen with the MDZ substrate. Interestingly, in a previous study, we have seen that P450cam displays dramatically narrower distance distributions using BSL labeling compared with that for monofunctional labeling,[5] while for CYP3A4, the width of the distance distribution between BSL and MTSL does not differ very much. This

suggests that the mode of spin labeling contributes less to the overall distance distribution in CYP3A4, perhaps as a result of higher flexibility in the protein structure itself.

Upon binding of the type I ligand, MDZ, the DEER modulation amplitude is largely lost and three weak peaks are observed with no single distance dominating. One potential explanation for this increased heterogeneity is that two or more molecules could enter the active site when MDZ is present in large excess, leading to F–G fragment heterogeneity. The 2-, 13-, and 100-fold MDZ samples show similar heterogeneity, suggesting the coexistence of multiple states. MDZ triggers an observable active site reshaping and involves the movements on the F–G segment that are far from the active site. Superposition of three crystallographically independent molecules present in the unit cell suggests that R243 is somewhat mobile, with Cα fluctuations of 0.8–1.2 Å. It is known that increasing mobility of the spin-labels results in a smaller modulation depth of the DEER. Therefore, our interpretation is that MDZ may be causing additional mobility of the spin-labels and the flexible binding pocket may allow multiple MDZ binding within the substrate channel resulting in conformational heterogeneity. Our MD distance distributions nicely coincide with the DEER result, where spin-label rotamers contribute to the DEER distance, and provide further supporting evidence of the increased structural flexibility of CYP3A4 after MDZ binding (Figure 4C). Moreover, the changes between ligand-free and MDZ-bound states seen by crystallography are clearly captured by MD, with the exception of that little difference in the G helix tip. In addition, MD shows larger differences in the E/F- and H/I-connecting loops compared to crystallography. Finally, the distance distributions extracted from MD runs show that the distribution width for the MDZ-bound state is twice as large as for the ligand-free form. Still, the widths seen in the DEER data are even greater than this but with a similar trend. These findings suggest that an increase in the conformational flexibility and mobility of the F–G fragment might be required to assist MDZ binding with the proper orientation and/or dissociation of the oxidized product.

CONCLUSION

The purpose of this study was to investigate how conformational dynamics of CYP3A4 respond to inhibitor and substrate binding in solution. This is important because CYP3A4 is capable of accommodating a wide range of structurally diverse ligands. Most CYP3A4/ligand co-crystal structures display less pronounced conformational changes that, in part, could be due to spatial constraints imposed by the crystal lattice. To overcome this problem, we utilized DEER methodology to obtain information about the intramolecular distance distribution and conformational ensemble of CYP3A4 in solution. Our results reveal ligand-dependent changes in the conformational mobility of CYP3A4, particularly at the outer surface of the active site. The binding of substrates and inhibitors was found to have a stronger stabilizing effect on the active site dynamics than the overall structure, which may give the enzyme an advantage in versatility and adaptability to the wide variety of substrates and facilitate product dissociation.

■ ASSOCIATED CONTENT

ⓈSupporting Information

The Supporting Information is available free of charge on the ACS Publications website at DOI: 10.1021/acs.biochem.9b00620.

Gel filtration elution profiles for Δ3−22 CYP3A4 at different CHAPS concentrations, UV−vis and CW-EPR spectra of Δ3−22 CYP3A4 with MTSL or BSL in different ligand-bound states, time evolution of nitroxide distance changes upon releasing DEER restraints for the MDZ-bound complex, comparison of DEER and MD distance distributions for BSL-labeled ligand-free Δ3−22 CYP3A4, overlay of MD and ligand-free crystal structures, MD-derived sampling of spin-label rotamers, background subtraction and L curves for DEER data, and validation of DEER distance distributions for MTSL-labeled Δ3−22 CYP3A4 in different ligand-bound states (PDF)

Accession Codes

Cytochrome P450 3A4 (CYP3A4), P08684.

■ AUTHOR INFORMATION

Corresponding Author

*E-mail: dbgoodin@ucdavis.edu.

ORCID ⬤

Shu-Hao Liou: 0000-0002-9716-6108
Lee-Ping Wang: 0000-0003-3072-9946
R. David Britt: 0000-0003-0889-8436
Thomas L. Poulos: 0000-0002-5648-3510
Irina F. Sevrioukova: 0000-0002-4498-6057
David B. Goodin: 0000-0002-9196-0001

Author Contributions

D.B.G., I.F.S., S.-H.L., and S.-W.C. designed the research. I.F.S., S.-H.L., and S.-W.C. performed the research. S.-W.C. and D.B.G. analyzed the data. T.L.P., R.D.B., and L.-P.W. advised on the analysis and interpretation. S.-W.C., I.F.S., T.L.P., and D.B.G. wrote the paper.

Notes

The authors declare no competing financial interest.

■ ABBREVIATIONS

CW, continuous wave; DEER, double electron−electron resonance; MD, molecular dynamics; MTSL, (1-oxyl-2,2,5,5-tetramethylpyrroline-3-methyl) methanethiosulfonate; BSL, 3,4-bis(methanethiosulfonylmethyl)-2,2,5,5-tetramethyl-2,5-dihydro-1H-pyrrol-1-yloxy spin-label; KET, ketoconazole; RIT, ritonavir; MDZ, midazolam; CHAPS, 3-[(3-cholamidopropyl)-dimethylammonio]-1-propanesulfonate; CYP3A4, cytochrome P450 3A4; EPR, electron paramagnetic resonance.

■ REFERENCES

(1) Guengerich, F. P. (1999) Cytochrome P-450 3A4: regulation and role in drug metabolism. *Annu. Rev. Pharmacol. Toxicol. 39*, 1−17.
(2) Conner, K. P., Woods, C. M., and Atkins, W. M. (2011) Interactions of cytochrome P450s with their ligands. *Arch. Biochem. Biophys. 507*, 56−65.

(3) Sligar, S. G., and Gunsalus, I. C. (1976) A thermodynamic model of regulation: modulation of redox equilibria in camphor monooxygenase. *Proc. Natl. Acad. Sci. U. S. A. 73*, 1078−1082.
(4) Sligar, S. G. (1976) Coupling of spin, substrate, and redox equilibria in cytochrome P450. *Biochemistry 15*, 5399−5406.
(5) Liou, S.-H., Mahomed, M., Lee, Y.-T., and Goodin, D. B. (2016) Effector Roles of Putidaredoxin on Cytochrome P450cam Conformational States. *J. Am. Chem. Soc. 138*, 10163−10172.
(6) Stoll, S., Lee, Y. T., Zhang, M., Wilson, R. F., Britt, R. D., and Goodin, D. B. (2012) Double electron-electron resonance shows cytochrome P450cam undergoes a conformational change in solution upon binding substrate. *Proc. Natl. Acad. Sci. U. S. A. 109*, 12888−12893.
(7) Gay, S., Sun, L., Maekawa, K., Halpert, J., and Stout, C. D. (2009) Crystal Structures of Cytochrome P450 2B4 in Complex with the Inhibitor 1-Biphenyl-4-methyl-1 H-imidazole: Ligand-Induced Structural Response through α-Helical Repositioning. *Biochemistry 48*, 4762−4771.
(8) Schoch, G. A., Yano, J. K., Wester, M. R., Griffin, K. J., Stout, C. D., and Johnson, E. F. (2004) Structure of Human Microsomal Cytochrome P450 2C8: Evidence For A Peripheral Fatty Acid Binding Site. *J. Biol. Chem. 279*, 9497−9503.
(9) Yano, J. K., Hsu, M.-H., Griffin, K. J., Stout, C. D., and Johnson, E. F. (2005) Structures of human microsomal cytochrome P450 2A6 complexed with coumarin and methoxsalen. *Nat. Struct. Mol. Biol. 12*, 822−823.
(10) Yano, J. K., Denton, T. T., Cerny, M. A., Zhang, X., Johnson, E. F., and Cashman, J. R. (2006) Synthetic Inhibitors of Cytochrome P-450 2A6: Inhibitory Activity, Difference Spectra, Mechanism of Inhibition, and Protein Cocrystallization. *J. Med. Chem. 49*, 6987−7001.
(11) Sansen, S., Hsu, M.-H., Stout, C. D., and Johnson, E. F. (2007) Structural insight into the altered substrate specificity of human cytochrome P450 2A6 mutants. *Arch. Biochem. Biophys. 464*, 197−206.
(12) Schoch, G. A., Yano, J. K., Sansen, S., Dansette, P. M., Stout, C. D., and Johnson, E. F. (2008) Determinants of Cytochrome P450 2C8 Substrate Binding: Structures Of Complexes With Montelukast, Troglitazone, Felodipine, and 9-Cis-Retinoic Acid. *J. Biol. Chem. 283*, 17227−17237.
(13) Sevrioukova, I. F., and Poulos, T. L. (2010) Structure and mechanism of the complex between cytochrome P4503A4 and ritonavir. *Proc. Natl. Acad. Sci. U. S. A. 107*, 18422−18427.
(14) Ekroos, M., and Sjögren, T. (2006) Structural basis for ligand promiscuity in cytochrome P450 3A4. *Proc. Natl. Acad. Sci. U. S. A. 103*, 13682−13687.
(15) Yano, J. K., Wester, M. R., Schoch, G. A., Griffin, K. J., Stout, C. D., and Johnson, E. F. (2004) The structure of human microsomal cytochrome P450 3A4 determined by X-ray crystallography to 2.05-A resolution. *J. Biol. Chem. 279*, 38091−38094.
(16) Williams, P. A., Cosme, J., Vinkovic, D. M., Ward, A., Angove, H. C., Day, P. J., Vonrhein, C., Tickle, I. J., and Jhoti, H. (2004) Crystal structures of human cytochrome P450 3A4 bound to metyrapone and progesterone. *Science 305*, 683−686.
(17) Thummel, K. E., and Wilkinson, G. R. (1998) In vitro and in vivo drug interactions involving human CYP3A. *Annu. Rev. Pharmacol. Toxicol. 38*, 389−430.
(18) Sevrioukova, I. F., and Poulos, T. L. (2017) Structural basis for regiospecific midazolam oxidation by human cytochrome P450 3A4. *Proc. Natl. Acad. Sci. U. S. A. 114*, 486−491.
(19) Ekroos, M., and Sjogren, T. (2006) Structural basis for ligand promiscuity in cytochrome P450 3A4. *Proc. Natl. Acad. Sci. U. S. A. 103*, 13682−13687.
(20) Sevrioukova, I. F., and Poulos, T. L. (2010) Structure and mechanism of the complex between cytochrome P4503A4 and ritonavir. *Proc. Natl. Acad. Sci. U. S. A. 107*, 18422−18427.
(21) Sevrioukova, I. F., and Poulos, T. L. (2015) Anion-Dependent Stimulation of CYP3A4Monooxygenase. *Biochemistry 54*, 4083−4096.

(22) Denisov, I. G., Baas, B. J., Grinkova, Y. V., and Sligar, S. G. (2007) Cooperativity in cytochrome P450 3A4: linkages in substrate binding, spin state, uncoupling, and product formation. *J. Biol. Chem.* 282, 7066−7076.

(23) Bayburt, T. H., and Sligar, S. G. (2010) Membrane protein assembly into Nanodiscs. *FEBS Lett.* 584, 1721−1727.

(24) Sevrioukova, I. F. (2017) High-Level Production and Properties of the Cysteine-Depleted Cytochrome P450 3A4. *Biochemistry* 56, 3058−3067.

(25) Jeschke, G., Chechik, V., Ionita, P., Godt, A., Zimmermann, H., Banham, J., Timmel, C. R., Hilger, D., and Jung, H. (2006) DeerAnalysis2006—a comprehensive software package for analyzing pulsed ELDOR data. *Appl. Magn. Reson.* 30, 473−498.

(26) Frisch, M. J., Trucks, G. W., Schlegel, H. B., Scuseria, G. E., Robb, M. A., Cheeseman, J. R., Scalmani, G., Barone, V., Petersson, G. A., Nakatsuji, H., Li, X., Caricato, M., Marenich, A. V., Bloino, J., Janesko, B. G., Gomperts, R., Mennucci, B., Hratchian, H. P., Ortiz, J. V., Izmaylov, A. F., Sonnenberg, J. L., Williams, Ding, F., Lipparini, F., Egidi, F., Goings, J., Peng, B., Petrone, A., Henderson, T., Ranasinghe, D., Zakrzewski, V. G., Gao, J., Rega, N., Zheng, G., Liang, W., Hada, M., Ehara, M., Toyota, K., Fukuda, R., Hasegawa, J., Ishida, M., Nakajima, T., Honda, Y., Kitao, O., Nakai, H., Vreven, T., Throssell, K., Montgomery, J. A., Jr., Peralta, J. E., Ogliaro, F., Bearpark, M. J., Heyd, J. J., Brothers, E. N., Kudin, K. N., Staroverov, V. N., Keith, T. A., Kobayashi, R., Normand, J., Raghavachari, K., Rendell, A. P., Burant, J. C., Iyengar, S. S., Tomasi, J., Cossi, M., Millam, J. M., Klene, M., Adamo, C., Cammi, R., Ochterski, J. W., Martin, R. L., Morokuma, K., Farkas, O., Foresman, J. B., and Fox, D. J. (2016) *Gaussian 09*, Gaussian, Inc., Wallingford, CT.

(27) Wang, J., Wang, W., Kollman, P. A., and Case, D. A. (2006) Automatic atom type and bond type perception in molecular mechanical calculations. *J. Mol. Graphics Modell.* 25, 247−260.

(28) Bayly, C. I., Cieplak, P., Cornell, W., and Kollman, P. A. (1993) A well-behaved electrostatic potential based method using charge restraints for deriving atomic charges: the RESP model. *J. Phys. Chem.* 97, 10269−10280.

(29) Li, P., and Merz, K. M. (2016) MCPB.py: A Python Based Metal Center Parameter Builder. *J. Chem. Inf. Model.* 56, 599−604.

(30) Wang, J., Wolf, R. M., Caldwell, J. W., Kollman, P. A., and Case, D. A. (2004) Development and testing of a general amber force field. *J. Comput. Chem.* 25, 1157−1174.

(31) Maier, J. A., Martinez, C., Kasavajhala, K., Wickstrom, L., Hauser, K. E., and Simmerling, C. (2015) ff14SB: Improving the Accuracy of Protein Side Chain and Backbone Parameters from ff99SB. *J. Chem. Theory Comput.* 11, 3696−3713.

(32) Roe, D. R., and Cheatham, T. E. (2013) PTRAJ and CPPTRAJ: Software for Processing and Analysis of Molecular Dynamics Trajectory Data. *J. Chem. Theory Comput.* 9, 3084−3095.

(33) Case, D. A., Cerutti, D. S., Cheatham, I., Darden, T., Giese, T. J., Gohlke, H., Goetz, A. W., Greene, D., Homeyer, N., Izadi, S., Kovalenko, A., Lee, T. S., LeGrand, S., Li, P., Lin, C., Liu, J., Luchko, T., Luo, R., Mermelstein, D., Merz, K. M., Monard, G., Nguyen, H., Omelyan, I., Onufriev, A., Pan, F., Qi, R., Roe, D. R., Roitberg, A., Sagui, C., Simmerling, C. L., Botello-Smith, W. M., Swails, J., Walker, R. C., Wang, J., Wolf, R. M., Wu, X., Xiao, L., York, D. M., and Kollman, P. A. (2017) *AMBER16*, University of California, San Francisco.

(34) Dawson, J. H., Andersson, L. A., and Sono, M. (1982) Spectroscopic investigations of ferric cytochrome P-450-CAM ligand complexes. Identification of the ligand trans to cysteinate in the native enzyme. *J. Biol. Chem.* 257, 3606−3617.

(35) Roberts, A. G., Campbell, A. P., and Atkins, W. M. (2005) The Thermodynamic Landscape of Testosterone Binding to Cytochrome P450 3A4: Ligand Binding and Spin State Equilibria. *Biochemistry* 44, 1353−1366.

(36) Davydov, D. R., Davydova, N. Y., Sineva, E. V., Kufareva, I., and Halpert, J. R. (2013) Pivotal role of P450−P450 interactions in CYP3A4 allostery: the case of α-naphthoflavone. *Biochem. J.* 453, 219−230.

(37) Davydov, D., Davydova, N., Sineva, E., and Halpert, J. (2015) Interactions among Cytochromes P450 in Microsomal Membranes. *J. Biol. Chem.* 290, 3850−3864.